Received: 29 October 2020 | Revised: 20 January 2021 | Accepted: 26 March 2021

DOI: 10.1002/fld.4984

RESEARCH ARTICLE

WILEY

Phase-field formulation of a fictitious domain method for particulate flows interacting with complex and evolving geometries

Martin Reder[1,2] | **Daniel Schneider**[1,2] | **Fei Wang**[2] | **Simon Daubner**[2] | **Britta Nestler**[1,2]

[1] Institute of Digital Materials Science, Karlsruhe University of Applied Sciences, Karlsruhe, Germany

[2] Institute of Applied Materials-Computational Materials Science, Karlsruhe Institute of Technology, Karlsruhe, Germany

Correspondence
Martin Reder, Institute of Digital Materials Science, Karlsruhe University of Applied Science, Moltkestraße 30, Karlsruhe 76133, Germany.
Email: martin_dominik.reder@hs-karlsruhe.de

Funding information
Deutsche Forschungsgemeinschaft, Grant/Award Number: 390874152; Ministerium für Wissenschaft, Forschung und Kunst Baden-Württemberg

Abstract

A distributed Lagrange multiplier/fictitious domain method in a phase-field formulation for the simulation of rigid bodies in incompressible fluid flow is presented. The phase-field method yields an implicit representation of geometries and thus rigid body particulate flows within arbitrary geometries can be simulated based on a fixed Cartesian grid. Therefore, a phase-field based collision model is introduced in order to address contact of particles with arbitrary solid structures as boundaries. In addition, grain growth within the boundary geometry can be considered leading to changes in its shape during the simulation. The method is validated on benchmark problems and a convergence study is performed. Multiple numerical experiments are carried out in order to show the methods' capability to simulate problems with differently shaped rigid bodies and particulate flows involving complex boundary geometries like foam structures.

KEYWORDS

distributed Lagrange multiplier, fictitious domain, phase-field method, rigid body particulate flow, solid–fluid interaction

1 | INTRODUCTION

The motion of solid bodies in a surrounding fluid is a phenomenon widely observed in nature and engineering applications. Examples are sedimenting and fluidized suspensions, fluidized beds,[1] or sediment transport in rivers.

There are different approaches for the simulation of such solid–fluid interaction processes. Most are generally feasible for both rigid body and elastic representations of the solid. One group is body-fitted mesh methods like the arbitrary Lagrange–Euler (ALE) method,[2-4] where the grid is continuously adjusted to the solid bodies moving in the flow. The ALE method ensures that grid nodes of the solid and fluid always coincide at the interface. In order to adapt the grid to the body movement, a mesh moving scheme is used to displace grid nodes. This leads to a new reference configuration in the fluid domain, where the governing equations need to be mapped to. However, for large grid distortions, for example, in case of rotating bodies, a remeshing is necessary, leading to high computational costs especially for complex geometries. The remeshing also introduces errors from interpolating the fields onto the new grid.

Another group is based on a full Eulerian framework, where an Eulerian configuration is considered and discretized with a fixed grid. In this case, the solid domain and the location of the fluid–solid interface are not automatically tracked like for the body-fitted mesh methods. Therefore, an interface-tracking is required, what can be achieved via the volume-of-fluid method,[5] the level set method,[6,7] or a phase-field method.[8,9] One example of full Eulerian approaches is the immersed boundary method (IBM).[10,11] The idea is to solve the Navier–Stokes equation (NSE) in the whole computational domain and account for the solid via a body force, thus a decoupling of the fluid and solid problem is achieved. A second example in the context of a rigid body representation for the solid is the distributed Lagrange multiplier (DLM) method based on a fictitious domain.[12] A Lagrange multiplier field, that enforces a rigid body motion, is added to the fluid equations. This is incorporated into a monolithic weak formulation.[12] Patankar et al.[13] reformulated the method by using a constraint for the deformation-rate tensor, which is referred to as stress-DLM method. Sharma and Patankar[14] introduced a first-order stress-DLM in a finite volume formulation. Second-order formulations can be found in References 15,16.

The existing methods are capable of simulating rigid particulate flow with high numbers of particles, for example, Gallier et al.[17] consider 10,000 spherical particles falling within a three-dimensional rectangular domain. However, the particulate flow simulations did not involve further physical effects and were so far only considered within relatively simple boundary geometries like channels or pipes and without any obstacles inside the flow besides other spherical particles. In the present work, we present a method that can consider particulate flow within complex boundary geometries, like porous structures or foams, without the requirement of an expensive mesh generation for those cases. Therefore, the stress-DLM method by Sharma and Patankar[14] is adapted for the usage in conjunction with a phase-field method. The phase-field method introduces order parameters to distinguish between solid and fluid, and employs a diffuse interface in between. This offers the implicit parametrization of geometries on arbitrary grids without body-fitted meshes.[18] In addition, the phase-field method allows the tracking of the moving bodies and thus, especially nonspherical bodies can be considered without difficulty. It is also possible to consider phase transformation processes, for example, in the boundary geometry, which will change its shape with time. Also the rigid bodies themselves can be considered as growing crystals like in the work of Takaki et al.[19] The geometry parametrization via the phase-field method enables the treatment of both, the moving rigid bodies and an arbitrary boundary geometry, on a Cartesian grid without large computational overhead compared with a pure fluid flow. The usage of fixed Cartesian grids avoids mesh generation and potential remeshing. In addition, it enables the employment of efficient multigrid solvers for the pressure Poisson equation and a simple parallelization via domain decomposition. The present method was implemented in the PACE3D-software,[20] which provides a multiphysics framework in the phase-field context. A solver parallelization is performed via message-passing-interface.

The mathematical formulation of the method and the numerical discretization is introduced. Validation simulations are conducted in order to demonstrate the ability of the presented method to achieve the coupling of rigid body motion with the fluid flow. It is also shown, that it is possible to consider the interaction of particulate flows with boundary structures like foams. In addition, a simulation example with grain growth within the boundary geometry is given, with which the particulate flow interacts. As part of future work, we want to consider the rigid body motion within a multiphase flow, which has applications, for example, in the battery electrode manufacturing. The present framework offers a straightforward way to achieve this coupling, since the phase-field method is also established for the treatment of multiphase flow.[21]

2 | MATHEMATICAL FORMULATION

2.1 | Fluid-rigid-body interaction model

We consider N rigid bodies in an incompressible fluid flow. However, the method is in principle also applicable for compressible flows. The computational domain is denoted as Ω and the fluid and solid region with Ω_f and Ω_s, respectively. The solid region is the set union of all rigid body domains

$$\Omega_\mathrm{s} = \bigcup_{p=1}^{N} \Omega_p. \tag{1}$$

The governing equations are the momentum balance

$$\rho\dot{\vec{u}} = \rho\vec{f}_{\mathrm{V}} + \nabla\cdot\boldsymbol{\sigma} \tag{2}$$

and the corresponding kinematic constraints

$$\boldsymbol{D}(\vec{u}) = sym(\nabla\vec{u}) = \boldsymbol{0}, \quad \forall\vec{x}\in\Omega_{\mathrm{s}}, \tag{3}$$

$$\nabla\cdot\vec{u} = 0, \quad \forall\vec{x}\in\Omega_{\mathrm{f}}, \tag{4}$$

namely the rigidity constraint (3) in the solid domain and the continuity Equation (4) in the fluid. Herein, $\vec{u}$ is the velocity field, $\vec{x}$ a spacial point, ρ the mass density, $\vec{f}_{\mathrm{V}}$ a body force and $\boldsymbol{\sigma}$ the Cauchy stress tensor. The operator $sym(\cdot) = \frac{1}{2}[(\cdot) + (\cdot)^T]$ denotes the symmetrical part of a tensor and $\dot{(\cdot)} = \partial_t(\cdot) + \nabla(\cdot)\vec{u}$ the material time derivate. For incompressible flows, the pressure becomes a Lagrange multiplier that arises in order to achieve incompressibility by fulfilling the continuity equation. In a similar manner, the whole stress tensor acts as a Lagrange multiplier in the solid region, such that the rigidity is ensured. Subsequently, a Newtonian fluid with the dynamic viscosity μ is considered. However, the method is not restricted to this material behavior. The solution process for the coupled problem of rigid body motion and fluid flow is split in two steps. In a first step, the solid is represented by a ghost fluid and the Navier–Stokes system

$$\rho\dot{\vec{u}} = -\nabla p + \nabla\cdot\left[2\mu\boldsymbol{D}(\vec{u})\right] + \rho\vec{f}_{\mathrm{V}}, \tag{5a}$$

$$\nabla\cdot\vec{u} = 0 \tag{5b}$$

is solved in the whole domain. This yields the correct solution in the fluid region and a preliminary velocity field $\vec{u}^*$ in the solid. The motion of each rigid body is projected onto $\vec{u}^*$ under the assumption that the momentum and angular momentum are preserved.[13] The preliminary velocity field is used to determine the momentum $\vec{p}_p$ and the angular momentum $\vec{L}_p$ of the pth rigid body via

$$\vec{p}_p := m_p\vec{U}_p = \int_{\Omega_p}\rho\vec{u}^*\,\mathrm{d}V, \tag{6a}$$

$$\vec{L}_p := \boldsymbol{J}_p\vec{\omega}_p = \int_{\Omega_p}\rho\vec{r}_p\times\vec{u}^*\,\mathrm{d}V, \tag{6b}$$

with the mass m, the barycenter velocity $\vec{U}$, the angular velocity $\vec{\omega}$, and the rotational inertia

$$\boldsymbol{J}_p = \int_{\Omega_p}\rho(\vec{r}_p\cdot\vec{r}_p)\boldsymbol{1} - \rho\vec{r}_p\otimes\vec{r}_p\,\mathrm{d}V. \tag{7}$$

The unit tensor is denoted with $\boldsymbol{1}$ and $\vec{r}_p = \vec{x} - \vec{x}_p$ is the relative vector of a spacial point $\vec{x}$ to the barycenter. In the case of spherical bodies the deviatoric part of the inertia tensor vanishes, leading to $1/2\ mR^2\boldsymbol{1}$ in the two-dimensional and $2/5\ mR^2\boldsymbol{1}$ in three-dimensional case. Using (6), the barycenter velocity and angular velocity can be obtained, and with those the rigid body velocity field is calculated via

$$\vec{u} = \vec{U}_p + \vec{\omega}_p\times\vec{r}_p, \qquad \forall\vec{x}\in\Omega_p, \tag{8}$$

what satisfies the rigidity constraint (3). A detailed derivation of the employed DLM-formulation is given in Appendix A1. If an imposed motion of the rigid particles is considered, $\vec{U}_p$ and $\vec{\omega}_p$ are prescribed instead of being determined from Equation (6).

2.2 | Phase-field method and geometry parametrization

In order to distinguish between fluid and solid regions, the phase-field method is used. We introduce the phase variable $\varphi_\alpha(\vec{x})\in[0,1]$ representing the volume fraction of a phase α at all spacial points. At the interface between phases, the volume fraction exhibits a jump. However, in the phase-field method this jump is replaced by a diffuse interface with a steep but smooth transition of φ_α between 0 and 1 over a small region. This allows the interpolation of quantities to fulfill transition conditions. Generally, the phase-field is obtained via an evolution equation. It can be derived from a variational approach via the minimization of a total free energy functional.[22] The free energy functional reads

$$\mathcal{F} = \int_\Omega f_\mathrm{g}(\varphi_\alpha, \nabla\varphi_\alpha) + \psi(\varphi_\alpha) + f_\mathrm{b}(\varphi_\alpha)\,\mathrm{d}V, \tag{9}$$

where f_g is an energy contribution from phase-field gradients, ψ a potential, and f_b the energy contribution of bulk phases. Since they represent volume fractions, the phase variables of all N_α phases need to satisfy the summation constraint

$$\sum_{\alpha=1}^{N_\alpha} \varphi_\alpha(\vec{x}) = 1, \qquad \forall\,\vec{x}. \tag{10}$$

We employ the multiphase formulation of Nestler et al.[23] which yields the Allen–Cahn equation (ACE)

$$\dot{\varphi}_\alpha = -\kappa\frac{\delta\mathcal{F}}{\delta\varphi_\alpha} - \lambda, \tag{11}$$

for each phase α. Herein, $\delta(\cdot)$ denotes a variation, κ is a mobility, and λ a Lagrange multiplier, which makes sure the summation constraint (10) is satisfied. In a thermodynamic equilibrium the phase-field reaches its equilibrium-profile in the diffuse interface and the ACE reduces to the convective transport equation

$$\dot{\varphi}_\alpha = \partial_t\varphi_\alpha + \vec{u}\cdot\nabla\varphi_\alpha = 0. \tag{12}$$

This corresponds to the case of bodies, that change their shape only due to the given velocity field. In our case it is a rigid body velocity field, which will only lead to translation and rotation. However, the numeric solution of (12) introduces discretization errors, that will change the profile and interface width. Therefore, even if no phase transformation is considered, the right-hand side of the ACE needs to be incorporated in order to recover the equilibrium profile. This is not required every time step, but only when the deviation becomes too large. Subsequently, the ACE is specified with the restriction to a quasi-two-phase case, which means, that a maximum of two phases occur at a single point. The gradient contribution can then be written as $f_g = a_1/2\ \nabla\varphi_\alpha\cdot\nabla\varphi_\alpha$ and the potential as $\psi = a_2\tilde{\psi}$, what yields

$$\dot{\varphi}_\alpha = \kappa\left(a_1\nabla^2\varphi_\alpha - a_2\partial_{\varphi_\alpha}\tilde{\psi} + f_{\alpha\beta}\right). \tag{13}$$

The coefficients a_1 and a_2 depend on the potential. Let δ_I be the interface width and $\gamma_{\alpha\beta}$ the surface tension of the interface between phase α and β, then $a_1 \propto \gamma_{\alpha\beta}\delta_\mathrm{I}$ and $a_2 \propto \gamma_{\alpha\beta}/\delta_\mathrm{I}$ holds. The proportionality constants are chosen in such a way, that the surface energy is represented correctly, when an integration over the interface is performed. The term $f_{\alpha\beta}$ arises from the bulk energy difference between two phases and is a driving force for phase transformation from β in favor of α. In the case without phase transformation, the ACE has to be augmented with a Lagrange multiplier in order to preserve the volume (details see Reference 24) and curvature effects must be balanced out for shape preservation.[25] In the numerical experiments considered here, the ACE is used to treat the lamellar growth in the last example and it is used in its volume preserved form for the tracking of nonspherical rigid bodies. Note, that also the rigid body itself can be considered as a growing crystal with this formulation. For the special case of constant spherical rigid bodies, the usage of the evolution equation is an unnecessary effort. Instead, the phase-field can be directly prescribed using the equilibrium profile (see Figure 1). This leads to a similar approach to the surface digitizer introduced by Yuki et al.[26] There are different established choices for the potential in the ACE. The obstacle potential

$$\tilde{\psi} = \begin{cases} \varphi_\alpha\varphi_\beta & \vec{x}\in\partial\Omega_{\alpha\beta} \\ \infty & \text{otherwise} \end{cases} \tag{14}$$

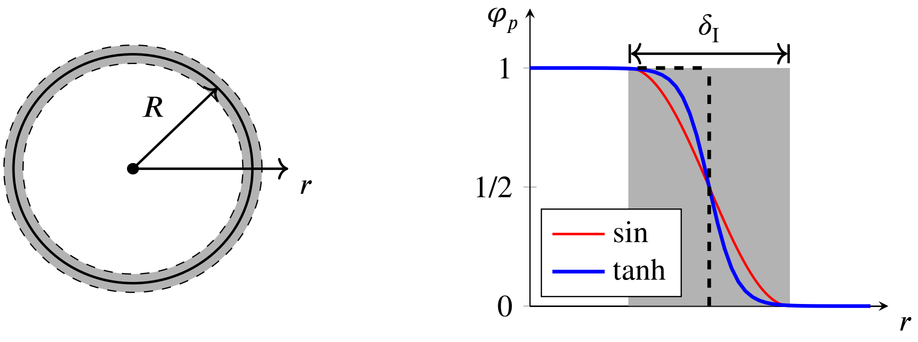

FIGURE 1 Prescription of the diffuse interface for a spherical particle [Colour figure can be viewed at wileyonlinelibrary.com]

leads to the equilibrium-profile

$$\varphi_p(\vec{x}) = \begin{cases} \frac{1}{2}\left[1 - \sin\left(\frac{\pi(r-R)}{\delta_\mathrm{I}}\right)\right] & R - \delta_\mathrm{I}/2 < r < R + \delta_\mathrm{I}/2 \\ 0 & r > R + \delta_\mathrm{I}/2 \\ 1 & r < R - \delta_\mathrm{I}/2 \end{cases} \tag{15}$$

where δ_I is the interface width, $r = \|\vec{r}_p\|$ the distance to the barycenter, and R the radius of the body. Alternatively, the well potential $\tilde{\psi} = \varphi_\alpha^2\varphi_\beta^2$ yields the equilibrium profile

$$\varphi_p(\vec{x}) = \frac{1}{2}\left[1 - \tanh\left(6\frac{r-R}{\delta_\mathrm{I}}\right)\right], \tag{16}$$

which has an asymptotic behavior. The interface width δ_I is described via a cut at $\varphi_p = 0.0025$ here. Both profiles are plotted in Figure 1 and can be used to prescribe the phase-field in case of constant spherical bodies. They only differ in the way, quantities are interpolated in the interface. We found no large impact of this choice on the solution for our test problems. Herein, the ACE is only used for nonspherical bodies and problems involving phase transformation processes. The prescribed profiles are used for the spherical case. In Appendix B1, a comparison of the different transport mechanisms is briefly discussed.

2.3 | Interface interpolation

The solution of the Navier–Stokes system is performed by means of multiphase flow, where the solid is represented by a ghost fluid at first. Therefore, the densities and the velocities are phase dependent, thus we have $\rho = \rho(\varphi_\alpha)$ and $\mu = \mu(\varphi_\alpha)$. In the diffuse interface region, an interpolation of those quantities is required. This can be done either by means of harmonic or arithmetic mean value yielding

$$\frac{1}{\rho} = \sum_{\alpha=1}^{N_\alpha}\frac{\varphi_\alpha}{\rho_\alpha} \quad \text{and} \quad \frac{1}{\mu} = \sum_{\alpha=1}^{N_\alpha}\frac{\varphi_\alpha}{\mu_\alpha}, \tag{17}$$

or

$$\rho = \sum_{\alpha=1}^{N_\alpha}\varphi_\alpha\rho_\alpha \quad \text{and} \quad \mu = \sum_{\alpha=1}^{N_\alpha}\varphi_\alpha\mu_\alpha, \tag{18}$$

respectively. Herein ρ_α and μ_α are the phase specific values. Moderate density- and viscosity-ratios of the phases lead to a low impact by the choice of the interpolation. If the phase-field solution satisfies the maximal principle, which is the case for solutions of the ACE, both interpolations are bounded above zero.[27,28] If the fluid flow itself is a multiphase flow, the NSE is augmented with an additional capillary term and is then given via

$$\rho\dot{\vec{u}} = -\nabla p + \nabla\cdot\left[\mu\left(\nabla\vec{u} + \nabla^T\vec{u}\right)\right] + \rho\vec{f}_\mathrm{V} - \sum_{\beta=1}^{\alpha}\sum_{\alpha=2}^{N_\alpha} a_2(\gamma_{\alpha\beta})\nabla\cdot(\nabla\varphi_\alpha\otimes\nabla\varphi_\alpha), \tag{19}$$

where $\gamma_{\alpha\beta}$ is the surface tension of the respective fluid interface.[21,29] In the diffuse interface between the fluid and a boundary structure, the adjustments of Beckermann et al.[30] are included in the NSE to correctly handle the no-slip condition. After the solution of the Navier–Stokes system is obtained, the velocity field of the rigid body motion is projected onto the preliminary solution in the rigid body domain. This needs some adjustments in the phase-field context, since the interfaces of two rigid bodies might overlap and the question of interpolation between the fluid and rigid body velocity arises. The velocity in the interface region is interpolated directly via

$$\vec{u} = \varphi_f \vec{u}^* + \sum_{p=1}^{N} \varphi_p \vec{u}_p, \tag{20}$$

where $\vec{u}_p = \vec{U}_p + \vec{\omega}_p \times \vec{r}_p$ denotes the rigid body velocity field of the pth body. The velocity correction for the rigid body domain then reads

$$\Delta \vec{u}' := \vec{u}^{n+1} - \vec{u}^* = \sum_{p=1}^{N} \varphi_p (\vec{U}_p + \vec{\omega}_p \times \vec{r}_p - \vec{u}^*). \tag{21}$$

The application of the projection (21) itself does not guarantee the preservation of momentum for a body, but introduces a difference due to the interpolation in the diffuse interface, which is quantified by

$$\Delta \vec{p}_p = \int_{\Omega} \rho_p \varphi_p \Delta \vec{u}' \, \mathrm{d}V. \tag{22}$$

This momentum difference can be balanced out again, which yields

$$\vec{u}^{n+1} = \vec{u}^* + \sum_{p=1}^{N} \left[\varphi_p (\vec{U}_p + \vec{\omega}_p \times \vec{r}_p - \vec{u}^*) - \frac{\Delta \vec{p}_p}{m_p} \right] \tag{23}$$

in the rigid body regions. The additional term for correcting the momentum depends on the interface width and thus the grid resolution. It will become very small for high resolutions.

2.4 | Collision model for particle–particle interaction

For the simulation of particulate flows a collision model is required, that handles contact between colliding solid surfaces. In theory, lubrication forces in the narrow gap between two surfaces prevent actual contact. However, in reality contact can still arise, for example, for low fluid viscosities and high approaching velocities of particles. Furthermore, the grid resolution is in general not high enough to sufficiently resolve the intersurface gap, and thus a collision or near collision model is mandatory.[31,32] Most collision models assume only spherical particles, since the width of the intersurface gap is easy to determine with the barycenter locations and the radii. So-called near collision models apply a distance dependent force, which counteracts further approaching of particles. A widely used model is the one of Glowinski et al.,[12] which applies the repelling force

$$\vec{F}_p = \begin{cases} -\tilde{c}\left(\frac{\delta - d}{\delta}\right)^2 \vec{n}_p & d < \delta \\ \vec{0} & \text{otherwise} \end{cases} \tag{24}$$

when particles get close to each other or the wall. Herein d is the distance between the surfaces, δ a distance proportional to the grid size, $\tilde{c}$ a scaling factor, that needs to be chosen, and $\vec{n}_p$ the outward pointing normal vector at the contact point. This models behavior strongly depends on the choice of the model parameter $\tilde{c}$ as it needs to be high enough to prevent overlapping.[3,15] At the same time, overly high repelling should be avoided due to an unphysical rebound. The parameter is problem dependent and cannot be given generally.

An alternative is a solid collision model, for example, the one of Johnson and Tezduyar.[4] It considers the equations for rigid body collision and thus neglects the fluid and the lubrication effects in between the solid surfaces. This is justified for a moderate fluid viscosity. The solid collision model has the advantage, that the only model parameter is the coefficient of restitution. If the particle velocities would lead to an overlapping during the current time step, a correction is applied according to

$$\vec{U}_p' = \vec{U}_p + \frac{(1+e)m_q}{m_p + m_q}(\vec{U}_q - \vec{U}_p) \cdot \vec{n}_p\, \vec{n}_p, \tag{25a}$$

$$\vec{U}_q' = \vec{U}_q + \frac{(1+e)m_p}{m_p + m_q}(\vec{U}_p - \vec{U}_q) \cdot \vec{n}_q\, \vec{n}_q. \tag{25b}$$

For collision with walls $m_q \to \infty$ and $\vec{U}_q = \vec{0}$ is used to obtain the collision equation

$$\vec{U}_p' = \vec{U}_p - (1+e)\vec{U}_p \cdot \vec{n}_p\, \vec{n}_p. \tag{26}$$

In order to cover multiple simultaneous collisions during a time step, an iterative algorithm checking for solid contact is employed. For spherical particles one of those models can be used.

2.5 | Model for contact with arbitrary solid structures

Since we want to consider particulate flow in conjunction with boundary geometries, a model for collision of particles with arbitrary structures is introduces, that makes use of the phase-field method. We consider some arbitrarily shaped solid obstacles inside the flow, with whom rigid bodies might collide. In such a case, the task is to identify contact between solid surfaces and determine the contact point in order to apply the collision model. With the phase-field method, the surface of a body is represented by the isosurface of $\varphi_\alpha = 1/2$. The product of two phase variables is an indicator of the distance in between the solid surfaces. In particular for the contact point $\varphi_p\varphi_q = 1/4$ is obtained (see Figure 2). Let q denote the index of a fixed solid obstacle, then

$$\varphi_p\varphi_q \geq \frac{1}{4} - c_\mathrm{t} \ \wedge \ \vec{U}_p \cdot \vec{n}_p \geq 0, \tag{27}$$

is used as a criterion for the application of the collision model, where c_t is a tolerance value, for example, 1/20. The algorithm goes through all cells and if the criterion (27) holds, the velocity correction

$$\vec{U}_p' = \vec{U}_p - 4\varphi_p\varphi_q(1+e)(\vec{U}_p \cdot \vec{n}_p)\, \vec{n}_p \tag{28}$$

is applied and the loop continues. This procedure enables the model to handle situations, where contact arises at multiple different points simultaneously for one rigid body. The second condition in (27) ensures, that the velocity is only corrected, if the particle would move towards the wall without a correction. This prevents a double correction in case of two neighboring cells with $\varphi_p\varphi_q \geq 1/4 - c_\mathrm{t}$. Note, that this procedure for contact with arbitrary geometries can easily be adjusted to a repelling force model. The distance between the surfaces is uniquely determined by the product $\varphi_p\varphi_q$ if the shape of the profile is known and hence the separation forces can be determined.

2.6 | Numerical discretization and computational algorithm

The considered partial differential equations (PDEs) are solved on a Cartesian grid with a conserving finite difference method. The velocity components are located at the corresponding face midpoints of each cell and thus for the evaluation of the momentum balance a staggered grid is used. The position of the solution variables on the grid is shown in Figure 3. The explicit Euler method is employed for the time discretization. The Navier–Stokes system is solved using a Chorin-type projection method for the pressure.[33,34] We exemplarily specify the spacial discretization of the important terms for the

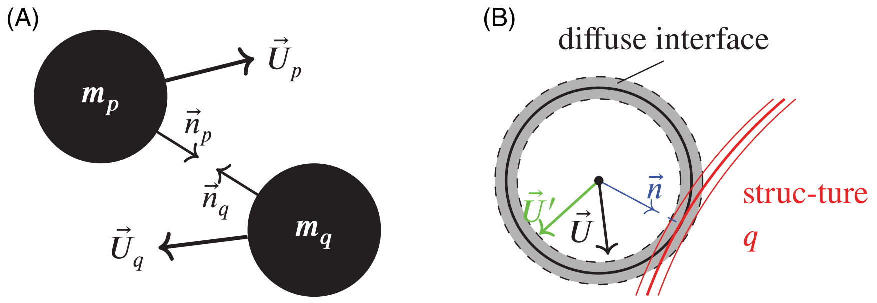

FIGURE 2 Schematic figure of solid contact. (A) Collision between two particles. (B) Contact with an arbitrary solid structure (red) inside the flow

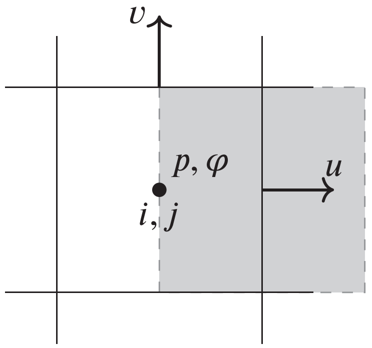

FIGURE 3 Positions of the field variables on the grid for cell i, j and control volume for the momentum balance in x-direction (gray)

x-component. The viscous term is discretized via

$$\frac{1}{\rho}\partial_x(\mu\partial_x u)\Big|_{i+1/2} \approx \frac{1}{\rho(\varphi_{i+1/2})\Delta x}\left(f_i^{\mathrm{diff}} - f_{i-1}^{\mathrm{diff}}\right) \tag{29}$$

with the flux

$$f_i^{\mathrm{diff}} = \mu(\varphi_i)\frac{u_{i+3/2} - u_{i+1/2}}{\Delta x}, \tag{30}$$

where density and viscosity are calculated using the arithmetic mean (17). A γ-scheme is employed for the convective term. It performs a blending between central differences and the first-order upwind scheme, which yields

$$\partial_x(u^2)|_{i+1/2} \approx \frac{1}{\Delta x}\left(f_i^{\mathrm{conv}} - f_{i-1}^{\mathrm{conv}}\right), \tag{31}$$

with the flux

$$f_i^{\mathrm{conv}} = u_{i+1}^{\mathrm{c}}\left[(1-\gamma)u_{i+1}^{\mathrm{c}} + \gamma u_{i+1}^{u}\right]. \tag{32}$$

The central and upwind approximations are

$$u_{i+1}^{\mathrm{c}} = \frac{1}{2}\left(u_{i+1/2} + u_{i+3/2}\right), \tag{33}$$

and

$$u_{i+1}^{\mathrm{u}} = \begin{cases} u_{i+1/2} & u_{i+1}^{\mathrm{c}} \geq 0 \\ u_{i+3/2} & u_{i+1}^{\mathrm{c}} < 0 \end{cases}, \tag{34}$$

respectively. The present method is first-order accurate in time and in between first and second order in space depending on the choice of γ. For $\gamma = 0$ it is formally second-order accurate. An overview over the computational algorithm is given subsequently, where the PDEs are written in semidiscrete form.

At the beginning of each time step $\vec{x}_p^n$, $\vec{U}_p^n$, $\vec{\omega}_p^n$, $\vec{u}^n$, p^n, and φ_α^n are known.

1. Solve the NSE without pressure

$$\vec{u}^{**} = \vec{u}^n + \Delta t \left[\frac{1}{\rho} \nabla \cdot (\mu \nabla \vec{u}) + \vec{f}_\mathrm{V} - \nabla \cdot (\vec{u} \otimes \vec{u}) \right] \Big|^n .$$

2. Solve the Poisson equation for the pressure

$$\nabla^2 p^{n+1} = \frac{\rho}{\Delta t} \nabla \cdot \vec{u}^{**}.$$

3. Use Chorins projection method to obtain the new velocity field

$$\vec{u}^* = \vec{u}^{**} - \frac{\Delta t}{\rho} \nabla p^{n+1}$$

and set $\vec{u}^{n+1} = \vec{u}^*$ in the fluid region.

4. Get the angular velocity and the barycenter velocity of each rigid body

$$\vec{U}_p^{n+1} = \frac{1}{m_p} \int_\Omega \rho_p \varphi_p^n \vec{u}^* \,\mathrm{d}V,$$
$$\vec{\omega}_p^{n+1} = \boldsymbol{J}_p^{-1} \int_\Omega \rho_p \varphi_p^n \vec{r}_p \times \vec{u}^* \,\mathrm{d}V.$$

5. Calculate the velocity difference due to rigid body presence

$$\Delta \vec{u}' = \sum_{p=1}^{N} \varphi_p (\vec{U}_p + \vec{\omega}_p \times \vec{r}_p - \vec{u}^*).$$

6. Correct the momentum deviation due to the diffuse interface

$$\Delta \vec{p}_p = \int_\Omega \rho_p \varphi_p \Delta \vec{u}' \,\mathrm{d}V.$$

7. Apply the new velocity field in the rigid body region

$$\vec{u}^{n+1} = \vec{u}^* + \sum_{p=1}^{N} \left[\varphi_p (\vec{U}_p + \vec{\omega}_p \times \vec{r}_p - \vec{u}^*) - \frac{\Delta \vec{p}_p}{m_p} \right].$$

8. Check for collisions and apply velocity changes accordingly.
9. Update the barycenter location via

$$\vec{x}_p^{n+1} = \vec{x}_p^n + \frac{1}{2} \left(\vec{U}_p^n + \vec{U}_p^{n+1} \right) \Delta t.$$

10. Update the phase-field to obtain φ_α^{n+1} via ACE or prescription

3 | NUMERICAL EXPERIMENTS AND VALIDATION

A number of numerical experiments are shown subsequently. The time step is chosen according to the maximum Courant number, such that $c := \Delta t \max(u_i(\vec{x})/\Delta x_i) \leq 0.2$ for the components $i = 1, 2, 3$. A value of 0.3 is used as the blending parameter of the γ-scheme, and thus it tends more towards central differences. In the subsequent simulations, the sin-type obstacle equilibrium profile is employed and the interface width δ_I is chosen as 2.5 times the spacial mean discretization

TABLE 1 Number of cells/time steps for the simulation setup and resulting Reynolds number

	$d/\Delta x$	n_x	n_y	n_z	n_t	Re_e
Coarse	12	80	80	128	4000	20.31
Middle	15	100	100	160	5000	20.87
Fine	18	120	120	192	6000	21.17

Note: The refinement factors are 1.25 from the coarse to the middle grid and 1.2 from the middle to the fine grid.

step size $h = \sqrt[3]{\Delta x \Delta y \Delta z}$ and $h = \sqrt{\Delta x \Delta y}$ in the three- and two-dimensional case, respectively. Interparticle collisions are modeled with the hard sphere contact model of Johnson and Tezduyar.[4] A preconditioned conjugated gradient method is employed for solving the linear system of the Poisson equation. The Gauß–Seidel method on a coarse grid with coarsening factor four is used for preconditioning. The residual for termination of the Poisson solver is 10^{-8}. The simulations were performed on a single core with an architecture based on Intel Xeon E5-2620 processors at 2.1 GHz. The computational time stated below refers to this setup. The usage of the parallelized code with more cores speeds up the simulations. However, the scaling behavior of the parallelized code was not yet investigated in detail.

3.1 | Falling sphere problem

In order to validate the method, a spherical particle falling under gravity is considered. The characteristic number in this case is the Archimedes number

$$Ar = \frac{\rho(\rho_p - \rho)d^3 g}{\mu^2},$$

where d is the particle diameter. A stationary particle end-velocity is reached when the gravity and drag forces are in equilibrium. For the simulations, the ratio of particle diameter and the cross domain width is $d/L = 0.15$ and the density ratio $\rho_p/\rho = 1.2$. We consider the Archimedes number $Ar = 800$. At the bottom of the domain a wall is considered and slip boundary conditions are applied at the other boundaries. A convergence study was conducted employing the Richardson extrapolation (RE) procedure (e.g., Cadafalch et al.[37]). The RE uses the results of three successively refined grids to estimate the order of accuracy $\hat{p}$ of the overall method and extrapolate a solution variable onto the grid independent solution $\hat{\phi}$. The hat indicates, that only an approximation of the respective quantity is obtained via the RE. Let ϕ_i be the value of a solution variable and h_i the discretization step size of the simulation on the ith grid, then a series expansion in terms of h yields the equations

$$\hat{\phi} = \phi_i + a h_i^{\hat{p}}, \qquad i = 1, 2, 3. \tag{35}$$

This results in three equations for the unknowns $\hat{\phi}$, $\hat{p}$, and a, that can be solved. The extrapolated solution $\hat{\phi}$ can be used as an error estimation for the discretization error, for example, in terms of the grid convergence index (GCI).[38] We consider three simulations with the spacial and temporal resolution given in Table 1. The RE is applied on the stationary particle velocities and yields the order of accuracy $\hat{p} = 1.93$, which is in good agreement with the theoretical order. A relative discretization error of 2.1% is estimated by means of the GCI for the fine grid solution. The solution of coarse and fine grid differs by 4% and the one between middle and fine grid by 1.4%. The falling sphere simulation was carried out with four different interface widths for the coarse and the middle resolution. The results are given in Table 2. The tendency is, that larger interfaces lead to higher drag in the solid–fluid interface and thus lower stationary end velocities. However, the impact of the interface width on the result decreases with the grid resolution.

The simulation results are compared with the theory. The force balance of drag and gravity yields the relationship

$$Re_e^2 = \frac{4Ar}{3c_d}$$

for the Reynolds number based on the particles' stationary velocity. The drag coefficient c_d is Reynolds number dependent and can be approximated, for example, with the Schiller–Naumann correlation[35]

$$c_d = \frac{24}{Re_e}(1 + 0.15 Re_e^{0.687})$$

TABLE 2 Variation of interface width

δ_I/h	2	2.5	3	3.5
Coarse	20.33	20.31	20.17	20.04
e_2^{rel}	0.11%	0.00%	−0.70%	−1.35%
Middle	20.826	20.813	20.807	20.797
e_2^{rel}	0.06%	0.00%	−0.03%	−0.07%

Note: Stationary Reynolds number Re_e and relative deviation e_2^{rel} regarding the case $\delta_I/h = 2.5$ for the coarse and middle resolution.

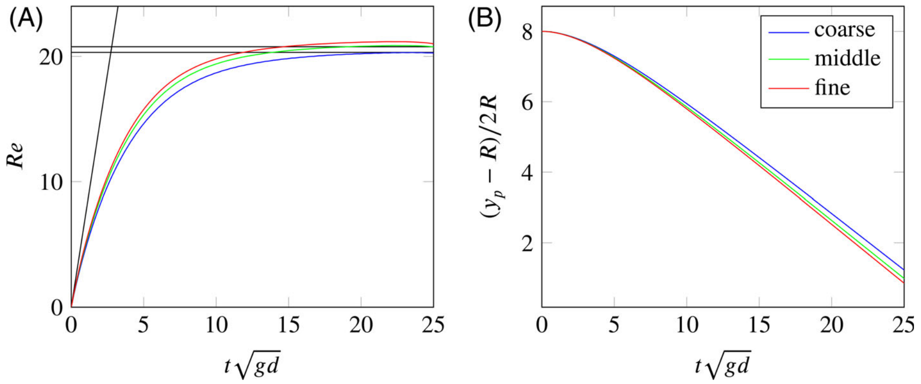

FIGURE 4 (A) Reynolds number of the falling sphere and comparison with values obtained from the correlations of Schiller and Naumann[35] and Brown and Lawler.[36] (B) Normalized height [Colour figure can be viewed at wileyonlinelibrary.com]

and thus the correlation

$$Re_e = \frac{Ar}{18 + 2.7Re_e^{0.687}} \tag{36}$$

between Reynolds number and Archimedes number is obtained for a falling sphere. This leads to the prediction of the Reynolds number $Re_e = 20.32$ in the stationary fall of the particle with Archimedes number $Ar = 800$. The correlation for the stationary velocity of Brown and Lawler[36] yields $Re_e = 20.77$ for that case. In addition, the initial acceleration of the sphere is analytically given via

$$\frac{\mathrm{d}U_p}{\mathrm{d}t} = \frac{\rho_p - \rho}{\rho_p + \rho/2} g. \tag{37}$$

A comparison of the simulations with the values of both considered empirical correlations are shown in Figure 4. The Reynolds number over time on the three different grids are depicted alongside the empirical stationary Reynolds number as well as the tangent of the initial acceleration. The deviation of the fine grid simulation result from the theoretical value are 4% and 2% compared with the correlations from References 35 and 36, respectively and thus good agreement is observed.

3.2 | Magnus effect for a rotating cylinder

As an example of forced rigid body motion, we consider the flow past a rotating cylinder at a Reynolds number $Re_\infty = 200$ and with the dimensionless rotational velocity $\tilde{\gamma} := \omega R/U_\infty$ in a range between 0 and 3. For the case without rotation, periodic Kármán vortex shedding occurs. Instabilities lead to the formation of vortexes in the cylinder wake, that separate with a certain frequency f, based on which the Strouhal number $St := 2\,Rf/U_\infty$ is defined. The rotation of the cylinder introduces an asymmetry, which leads to a nonvanishing mean value of the lift force in time, called Magnus effect.

For values of $\tilde{\gamma} > \tilde{\gamma}_c$ the vortex shedding disappears leading to a steady state solution. The experimental findings of Coutanceau and Ménard[40] determined γ_c to be around 2. Mittal and Kumar[39] report the critical value $\tilde{\gamma}_c = 1.91$. In our simulations, we observe shedding for $\tilde{\gamma} = 2$, while it is suppressed for $\tilde{\gamma} = 3$. The computational domain for the simulations is depicted in Figure 5 alongside the vorticity isolines for $\tilde{\gamma} = 1$, where the vortex shedding can be seen. Figure 6 depicts the

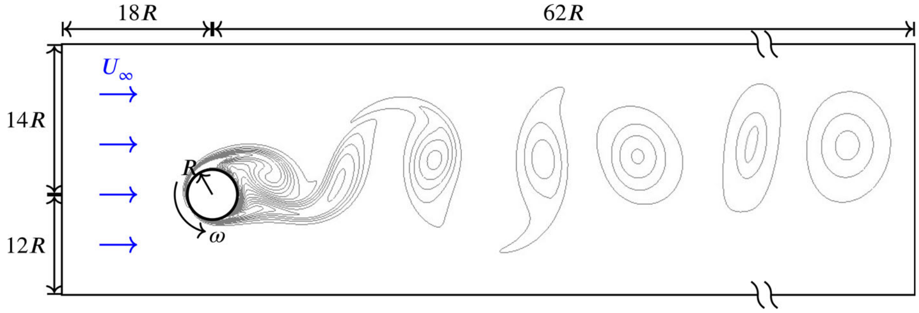

FIGURE 5 Computational domain and vorticity isolines for $\tilde{\gamma} = 1$ [Colour figure can be viewed at wileyonlinelibrary.com]

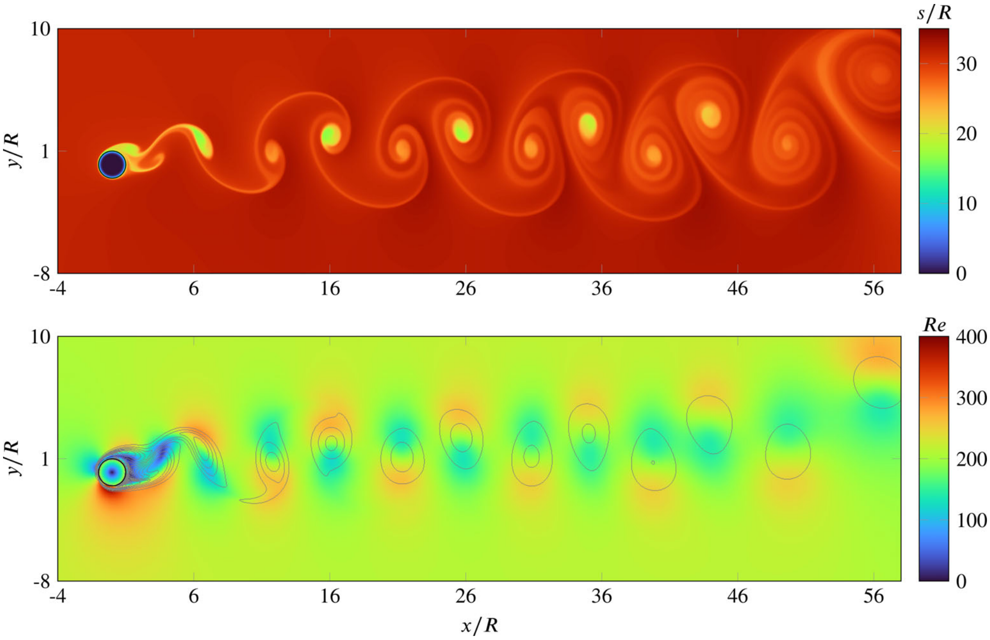

FIGURE 6 Results for $\tilde{\gamma} = 1$ slightly zoomed into the domain. Top: magnitude of displacement field. Bottom: vorticity isolines and local Reynolds number [Colour figure can be viewed at wileyonlinelibrary.com]

local Reynolds number based on the magnitude of the velocity field, the vorticity isolines, and the magnitude of the displacement field in Eulerian parametrization. The displacement field $\vec{s}$ is obtained from the inverse motion $\vec{\xi}$ via $\vec{s} = \vec{x} - \vec{\xi}$. The inverse motion maps the start location of a material point onto the spacial point it momentarily coincides with and it is obtained by solving

$$\dot{\vec{\xi}} = \vec{0}, \qquad \vec{\xi}(\vec{x}, t = 0) = \vec{x}.$$

This is done explicitly with an Euler method and a van Leer flux limiter scheme for the spacial discretization.

The displacement field is used to visualize the vortex structure in the wake. The time development of the lift coefficient c_l and the drag coefficient c_d is displayed in Figure 7. They are defined via

$$c_\mathrm{l} = \frac{\vec{F} \cdot \vec{e}_y}{\rho U_\infty^2 R},$$
$$c_\mathrm{d} = -\frac{\vec{F} \cdot \vec{e}_x}{\rho U_\infty^2 R},$$

where $\vec{e}_x$ and $\vec{e}_y$ are the unit vectors in x- and y-direction, and $\vec{F}$ is the force on the cylinder, which is normalized with the cylinder length. The normalized force is obtained by the line integral

$$\vec{F} = \int_{\partial \Omega_p} \boldsymbol{\sigma} \vec{n} \, \mathrm{d}l$$

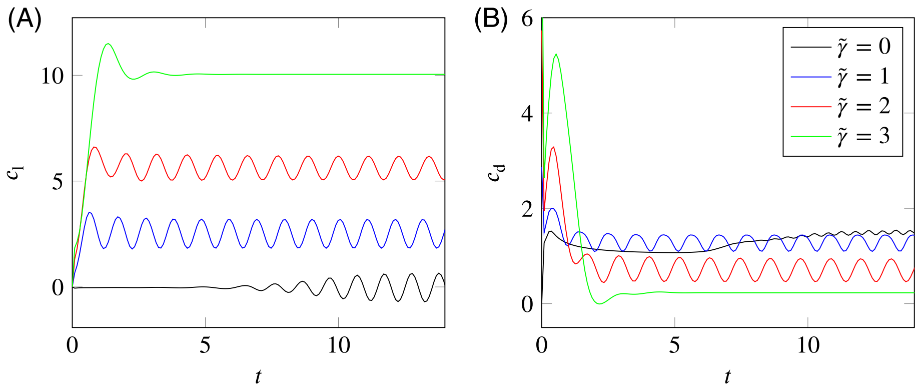

FIGURE 7 Time development of lift coefficient (A) and drag coefficient (B) for different angular velocities [Colour figure can be viewed at wileyonlinelibrary.com]

TABLE 3 Temporal mean values of lift c_l and drag c_d and Strouhal number St for different values of $\tilde{\gamma}$

	Present method			**Mittal and Kumar[39]**		
$\tilde{\gamma}$	***St***	$\overline{c_l}$	$\overline{c_d}$	***St***	$\overline{c_l}$	$\overline{c_d}$
0	0.1948	0.0	1.3298	0.1934	0.0	1.316
1	0.1922	2.5486	1.2952	0.1921	2.532	1.088
2	0.1758	5.6254	0.7009	–	5.358	0.298
3	–	10.0700	0.2285	–	10.316	0.043

Note: Comparison with data from Mittal and Kumar.[39]

over the contour of the sphere. Both lift and drag show oscillating behavior due to the vortex shedding. Only for $\tilde{\gamma} = 3$ the oscillations are damped immediately. The results of the present method are compared with data of Mittal and Kumar[39] in Table 3. They used a finite element formulation with a body-fitted mesh for their simulations. Lift and drag are compared by regarding their temporal mean values for the time interval, where the oscillations are fully developed. The temporal averaging is indicated with overbars. For $\tilde{\gamma} = 0$ and $\tilde{\gamma} = 1$ the deviation of the considered quantities is around 1%. For $\tilde{\gamma} = 2$ the results deviate especially for the drag, which is because Mittal and Kumar[39] find a critical value $\tilde{\gamma}_c = 1.91$, whereas in our simulations $\tilde{\gamma} = 2$ is still below the critical value, what explains the difference. Overall a good agreement is observed.

3.3 | Flow past a freely rotating cross

The treatment of nonspherical bodies is demonstrated via substitution of the rotating cylinder by a cross of the same size. The computational domain as well as the Reynolds number $Re_\infty = 200$ from the case above are maintained. The initial value for the angular velocity is set in order to obtain $\tilde{\gamma} = 1$ at $t = 0$. The cross is fixed in the center but can still freely rotate, and thus only $\vec{U} = \vec{0}$ is prescribed. We use the ACE with an obstacle potential for the phase-field evolution. However, the full ACE is only evaluated every 50th time step and otherwise the convective transport Equation (12) is solved. A van Leer flux limiter scheme is employed for the convective term. Figure 8 depicts the time development in respect to orientation and angular velocity of the cross. In addition, two snapshots of the velocity field near the cross are shown. Vortex shedding of the flow is also observed in this case. The cross undergoes some oscillatory rotation around the angle $\theta = \pi/2$. The angular velocity is damped away until the rotational direction changes. This is due to the torque introduced by the surface pressure difference arising from different orientations of the lower and upper arm of the cross in respect to the flow.

3.4 | Particles falling onto skew planes

To examine the model and its ability to handle collisions and prevent overlapping, we consider six different sized particles falling onto skew planes forming a cone. In this simulation the mean diameter of the particles is used as reference length

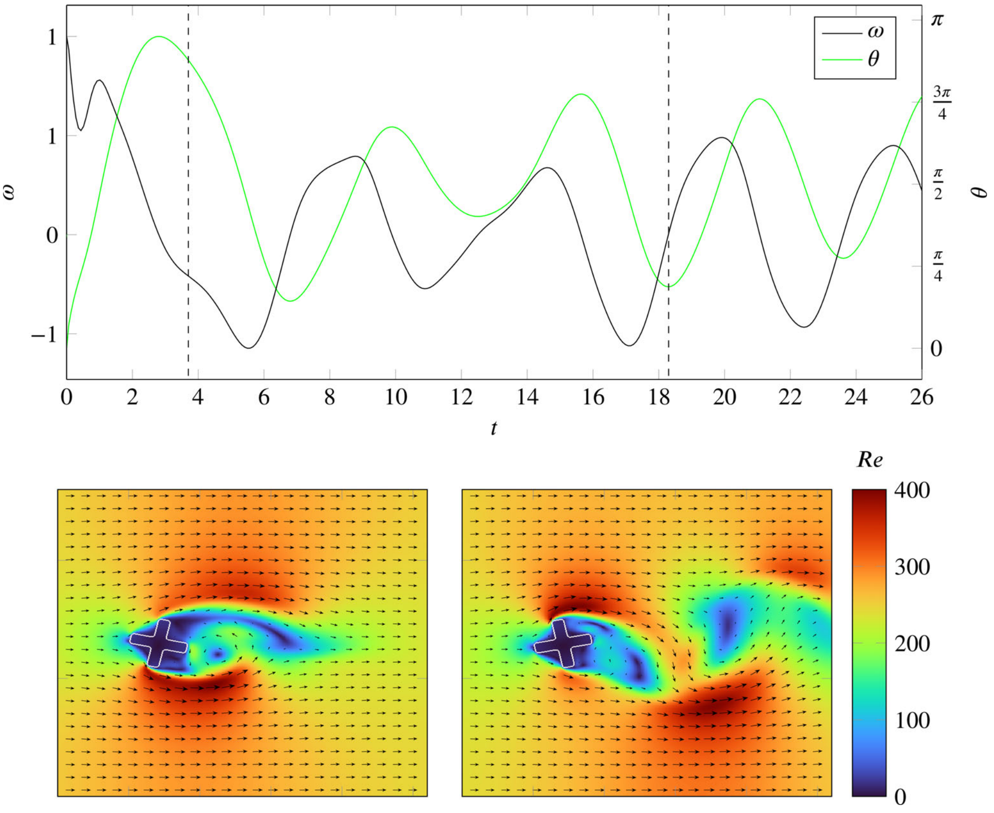

FIGURE 8 Flow past a freely rotating cross. Top: Time development of the angular velocity and the orientation of the cross. The dashed lines indicate the time from which the snapshots are taken. Bottom: Snapshots of the simulation showing the velocity field [Colour figure can be viewed at wileyonlinelibrary.com]

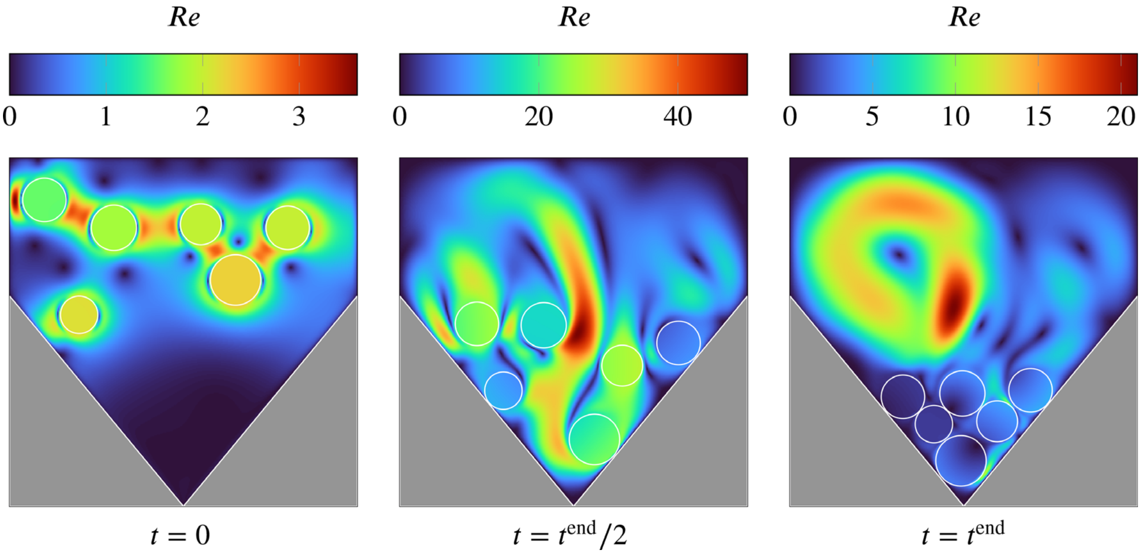

FIGURE 9 Snapshots of the simulation of particles falling onto skew planes. Isosurfaces of the respective phase-field and local Reynolds number based on the velocity magnitude [Colour figure can be viewed at wileyonlinelibrary.com]

and the considered Archimedes number is $Ar = 800$. The coefficient of restitution $e = 1$ is employed for the simulation. The domain is discretized with 400 cells in both x- and y-direction. The top and side boundaries are considered to be solid walls. Figure 9 shows snapshots for the simulation at different times. The Reynolds number is given based on the velocity magnitude and the mean diameter. The particles will collide with the wall, role further and eventually settle to the bottom of the cone. Their motion induces a vortex in the top left corner of the domain and a smaller one with opposed rotating direction in the top right. Both, collision of particles with the solid structure and with other particles are treated and overlapping is prevented even for multiple contact points simultaneously arising for one body.

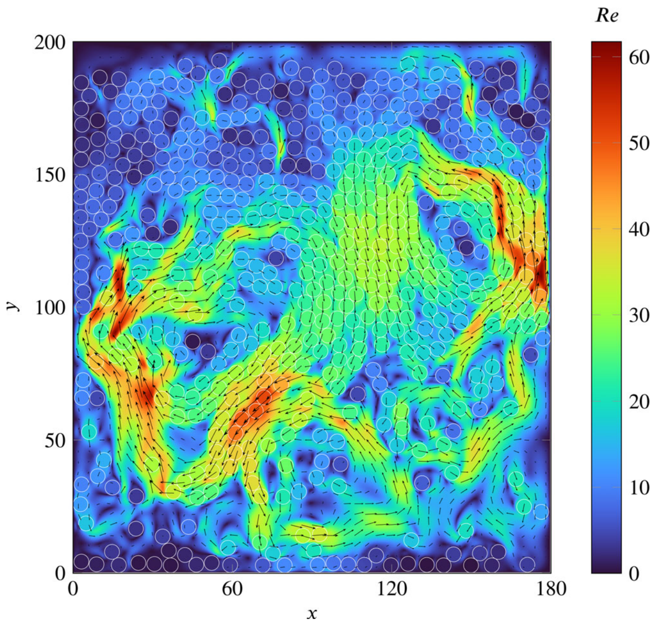

FIGURE 10 Fluidization of 504 spheres under gravity in a two-dimensional domain after 3000 time steps. Velocity field and particle shapes [Colour figure can be viewed at wileyonlinelibrary.com]

3.5 | Sedimentation of spheres in a closed box under gravity

A test problem involving a higher particle number is investigated next. We consider a setup consisting of a two-dimensional box with solid walls, where 504 spherical particles are initially distributed uniformly at the top of the box. The setup is similar to the ones in References 12,41. Since there are no quantitative results available for comparison, we only perform a qualitative investigation. The particles are released and fluidize under gravity. The Archimedes number is $Ar = 800$, the solid fraction is 34.48%, and the coefficient of restitution $e = 0.1$. The computational domain is discretized with $n_x \times n_y = 900 \times 1000$ cells. The simulation took 19 h with a total of 12,000 time steps. Figure 10 shows the velocity field and the particle contours by means of isolines with a phase variable value $\varphi = 0.5$. Further snapshots for the simulation can be found in Appendix B2. Rayleigh-Taylor instabilities lead to the formation of vortexes in the flow, and thus particles near the left and right wall get lifted temporarily, while particles in the middle of the domain fall down. The vortex formation leads to a mixing behavior of the particles before they settle at the bottom of the box.

3.6 | Particles falling into a three-dimensional foam structure

In order to demonstrate the methods potential in handling particulate flows interacting with complex boundary geometries, we consider a number of 32 spherical particles falling into a random generated three-dimensional foam structure as shown in Figure 11. The domain is discretized with $120 \times 120 \times 160$ cells in x-, y-, and z-direction, respectively. The simulation time was 51 h for a number of 10,000 time steps. The Archimedes number is chosen as $Ar = 800$ and the coefficient of restitution $e = 0.8$ is used. Fixed walls with $\vec{u} = \vec{0}$ are considered at the boundaries of the box. The time for a particle to reach the bottom of the domain depends strongly on the foam geometry determining the number of collisions one particle undergoes as well as the shortest way to the bottom. The fastest particle takes by factor 1.2 longer than a free fall over the same distance would take. This simulation showcases the present frameworks ability to simulate particulate flows interacting with solid structures, without limitation in respect to the considered geometry. The required calculation time is only weakly affected by the concrete nature of the geometry, since different ones can be treated on the same Cartesian grid. The only impact on the computational time is due to a geometry depending amount of collisions that occur. A higher number of collisions will also increase the computational cost.

3.7 | Channel flow with lamellar growth of the walls

Finally, we consider a channel flow at $Re = 200$ based on its initial height H and the bulk inflow velocity u_b. A parabolic velocity profile is considered as inflow condition. After a fix inflow region, the channel wall consists of a lamellar

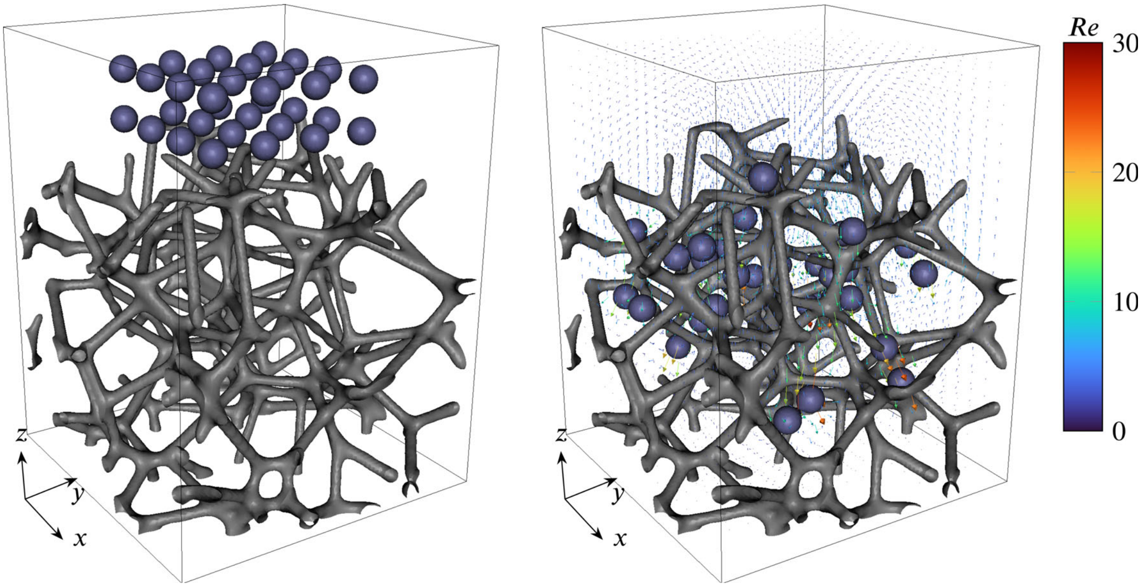

FIGURE 11 Particles falling into a foam structure. Left: initial setup. Right: snapshot after 5000 time steps [Colour figure can be viewed at wileyonlinelibrary.com]

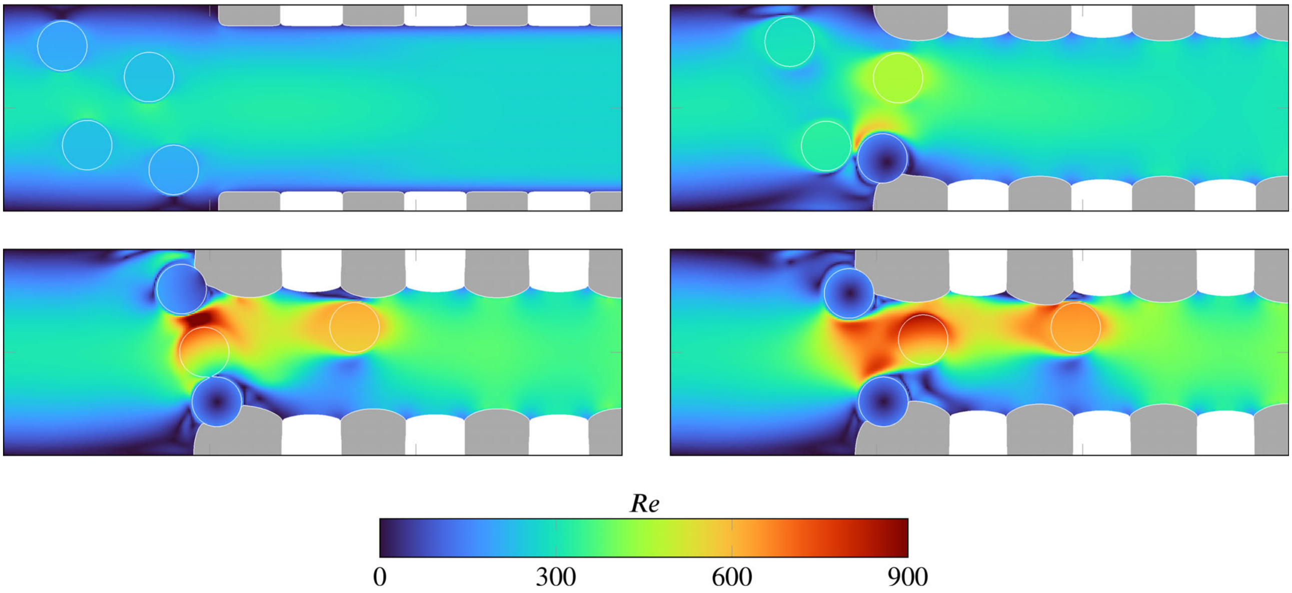

FIGURE 12 Velocity field and isosurfaces of the considered phases at different times from top left to bottom right [Colour figure can be viewed at wileyonlinelibrary.com]

arrangement of two solid phases, which grow into the fluid region with constant velocities that differ for both solid phases. The growth velocity of the solid front into the fluid is chosen to be 30% and 24% of the inflow bulk velocity for the solid phase 1 and 2, respectively. This is achieved by setting a constant bulk energy contribution f_{b} for each phase. The velocity is then obtained by multiplying the phasewise difference in f_{b} by the mobility κ, which is chosen to 1 here. The surface tension for all phases is constant and results in a Weber number $We = \rho u_{\mathrm{b}}^2 H/\gamma_{\alpha\beta} = 100$. Four spherical particles with diameter $d = H/4$ are placed inside the flow. Inelastic collisions with $e = 0$ are considered. Snapshots of the simulation are depicted in Figure 12. The particles hit the solid and are transported tangentially to the solid surface. At some point they can get stuck and the solid phase starts to grow around it. This is due to surface energy minimization. The simulation showcases the present frameworks potential of coupling particulate flow problems with phase transformation and grain growth.

Simulation	1	2	3	4	5
Navier–Stokes solution	99.34	99.41	98.29	71.27	98.20
Rigid body projection/collision	0.07	0.05	1.67	28.65	1.80
Calculation of inverse Motion	0.37	0.42	–	–	–
Allen–Cahn solution	–	0.11	–	–	–
Rest (data write out and so forth)	0.22	0.01	0.04	0.08	0.002

Note: Simulations: Magnus effect 1, rotating cross 2, particles falling into a cone 3, particles fluidizing in a box 4, particles falling into a foam structure 5.

TABLE 4 Contribution of different parts of the simulation process to the total computational time in %

3.8 | Distribution of computational time

A comparison of the computational cost arising from different parts of the simulation process for the considered numerical experiments is shown in Table 4. In all cases, the consumption of computational time is the largest for the solution of the Navier–Stokes system that is mostly arising from solving the Poisson equation. The contribution of the rigid body projection strongly depends on the number of considered particles and their total volume fraction. For the simulations with only a few bodies, the projection takes between 1% and 3% of the computational cost. For higher particle numbers the contribution of the rigid body projection rises, since the projection itself and the required integrations scale with the particle number times the number of cells, where a nonvanishing rigid phase occurs. In addition, the collision algorithm scales quadratic with the particle number. The simulation containing 504 particles shown in Figure B2 has already 30% of the computational cost required for the rigid body projection.

4 | CONCLUSIONS

We presented a DLM-type method for rigid body movement within fluid flow in a phase-field formulation. This approach offers a method for particulate flows within complex geometries that can be completely treated on a temporally constant Cartesian grid. The method was validated and is first-order accurate in time. However, the adjustment to second order is possible the same way like in Reference 15. The numerical experiments demonstrate the methods ability to consider nonspherical bodies as well as spherical particulate flow interacting with arbitrary structures and boundary geometries like foams. The phase-field framework also enables the boundary geometry to change, for example, due to grain growth and couple this process with the particulate flow, which was shown in one example. In addition, our framework allows the coupling of particulate flows with further physical effects. We plan to couple it with multiphase flow as part of future work.

ACKNOWLEDGMENTS

The authors gratefully acknowledge financial support by the Europäischer Fonds für regionale Entwicklung (EFRE) and the Ministerium für Wissenschaft, Forschung und Kunst Baden-Württemberg within the research center ZAFH InSeL. This work also contributes to the research performed at CELEST (Center for Electrochemical Energy Storage Ulm-Karlsruhe) funded by the German Research Foundation (DFG) under Project ID 390874152 (POLiS Cluster of Excellence).

DATA AVAILABILITY STATEMENT

The data that support the findings of this study are available from the corresponding author upon reasonable request.

ORCID

Martin Reder https://orcid.org/0000-0002-7503-9351

REFERENCES

1. Pan TW, Glowinski R, Galdi GP. Direct simulation of the motion of a settling ellipsoid in Newtonian fluid. *J Comput Appl Math*. 2002;149(1):71-82. https://doi.org/10.1016/S0377-0427(02)00521-6.
2. Basting S, Quaini A, Čanić S, Glowinski R. Extended ALE method for fluid–structure interaction problems with large structural displacements. *J Comput Phys*. 2017;331:312-336. https://doi.org/10.1016/j.jcp.2016.11.043.

3. Hu HH, Patankar NA, Zhu M. Direct numerical simulations of fluid–solid systems using the arbitrary Lagrangian–Eulerian technique. *J Comput Phys*. 2001;169(2):427-462. https://doi.org/10.1006/jcph.2000.6592.
4. Johnson AA, Tezduyar TE. Simulation of multiple spheres falling in a liquid-filled tube. *Comput Methods Appl Mech Eng*. 1996;134(3-4):351-373. https://doi.org/10.1016/0045-7825(95)00988-4.
5. Hirt CW, Nichols BD. Volume of fluid (VOF) method for the dynamics of free boundaries. *J Comput Phys*. 1981;39(1):201-225. https://doi.org/10.1016/0021-9991(81)90145-5.
6. Chang YC, Hou T, Merriman B, Osher S. A level set formulation of Eulerian interface capturing methods for incompressible fluid flows. *J Comput Phys*. 1996;124(2):449-464. https://doi.org/10.1006/jcph.1996.0072.
7. Sethian JA. *Level Set Methods and Fast Marching Methods: Evolving Interfaces in Computational Geometry, Fluid Mechanics, Computer Vision, and Materials Science*. Vol 3. Cambridge, MA: Cambridge University Press; 1999.
8. Fakhari A, Geier M, Bolster D. A simple phase-field model for interface tracking in three dimensions. *Comput Math Appl*. 2019;78:1154-1165. https://doi.org/10.1016/j.camwa.2016.08.021.
9. Sun Y, Beckermann C. Sharp interface tracking using the phase-field equation. *J Comput Phys*. 2007;220(2):626-653. https://doi.org/10.1016/j.jcp.2006.05.025.
10. Peskin CS. Flow patterns around heart valves: a numerical method. *J Comput Phys*. 1972;10(2):252-271. https://doi.org/10.1016/0021-9991(72)90065-4.
11. Bigot B, Bonometti T, Lacaze L, Thual O. A simple immersed-boundary method for solid–fluid interaction in constant- and stratified-density flows. *Comput Fluids*. 2014;97:126-142. https://doi.org/10.1016/j.compfluid.2014.03.030.
12. Glowinski R, Pan TW, Hesla TI, Joseph DD. A distributed Lagrange multiplier/fictitious domain method for particulate flows. *Int J Multiph Flow*. 1999;25(5):755-794. https://doi.org/10.1016/S0301-9322(98)00048-2.
13. Patankar NA, Singh P, Joseph DD, Glowinski R, Pan TW. A new formulation of the distributed Lagrange multiplier/fictitious domain method for particulate flows. *Int J Multiph Flow*. 2000;26(9):1509-1524. https://doi.org/10.1016/S0301-9322(99)00100-7.
14. Sharma N, Patankar NA. A fast computation technique for the direct numerical simulation of rigid particulate flows. *J Comput Phys*. 2005;205(2):439-457. https://doi.org/10.1016/j.jcp.2004.11.012.
15. Apte SV, Martin M, Patankar NA. A numerical method for fully resolved simulation (FRS) of rigid particle–flow interactions in complex flows. *J Comput Phys*. 2009;228(8):2712-2738. https://doi.org/10.1016/j.jcp.2008.11.034.
16. Veeramani C, Minev PD, Nandakumar K. A fictitious domain formulation for flows with rigid particles: a non-Lagrange multiplier version. *J Comput Phys*. 2007;224(2):867-879. https://doi.org/10.1016/j.jcp.2006.10.028.
17. Gallier S, Lemaire E, Lobry L, Peters F. A fictitious domain approach for the simulation of dense suspensions. *J Comput Phys*. 2014;256:367-387. https://doi.org/10.1016/j.jcp.2013.09.015.
18. Li X, Lowengrub J, Rätz A, Voigt A. Solving PDEs in complex geometries: a diffuse domain approach. *Commun Math Sci*. 2009;7(1):81-107. https://doi.org/10.4310/cms.2009.v7.n1.a4
19. Takaki T, Sato R, Rojas R, Ohno M, Shibuta Y. Phase-field lattice Boltzmann simulations of multiple dendrite growth with motion, collision, and coalescence and subsequent grain growth. *Comput Mater Sci*. 2018;147:124-131. https://doi.org/10.1016/j.commatsci.2018.02.004.
20. Hötzer J, Reiter A, Hierl H, Steinmetz P, Selzer M, Nestler B. The parallel multi-physics phase-field framework Pace3D. *J Comput Sci*. 2018;26:1-12. https://doi.org/10.1016/j.jocs.2018.02.011.
21. Jacqmin D. Calculation of two-phase Navier–Stokes flows using phase-field modeling. *J Comput Phys*. 1999;155(1):96-127. https://doi.org/10.1006/jcph.1999.6332.
22. Schneider D, Schwab F, Schoof E, et al. On the stress calculation within phase-field approaches: a model for finite deformations. *Comput Mech*. 2017;60(2):203-217. https://doi.org/10.1007/s00466-017-1401-8.
23. Nestler B, Garcke H, Stinner B. Multicomponent alloy solidification: phase-field modeling and simulations. *Phys Rev E*. 2005;71(4):041609. https://doi.org/10.1103/PhysRevE.71.041609.
24. Nestler B, Wendler F, Selzer M, Stinner B, Garcke H. Phase-field model for multiphase systems with preserved volume fractions. *Phys Rev E*. 2008;78(1):011604. https://doi.org/10.1103/PhysRevE.78.011604.
25. Schoof E, Schneider D, Streichhan N, Mittnacht T, Selzer M, Nestler B. Multiphase-field modeling of martensitic phase transformation in a dual-phase microstructure. *Int J Solids Struct*. 2018;134:181-194. https://doi.org/10.1016/j.ijsolstr.2017.10.032.
26. Yuki Y, Takeuchi S, Kajishima T. Efficient immersed boundary method for strong interaction problem of arbitrary shape object with the self-induced flow. *J Fluid Sci Technol*. 2007;2(1):1-11. https://doi.org/10.1299/jfst.2.1.
27. Liu C, Shen J. A phase field model for the mixture of two incompressible fluids and its approximation by a Fourier-spectral method. *Phys D Nonlinear Phenomena*. 2003;179(3-4):211-228. https://doi.org/10.1016/S0167-2789(03)00030-7.
28. Kim J. Phase-field models for multi-component fluid flows. *Commun Comput Phys*. 2012;12(3):613-661. https://doi.org/10.4208/cicp.301110.040811a.
29. Kim J, Lowengrub J. Phase field modeling and simulation of three-phase flows. *Interf Free Bound*. 2005;7(4):435-466. https://doi.org/10.4171/IFB/132.
30. Beckermann C, Diepers HJ, Steinbach I, Karma A, Tong X. Modeling melt convection in phase-field simulations of solidification. *J Comput Phys*. 1999;154(2):468-496. https://doi.org/10.1006/jcph.1999.6323.
31. Maury B. A many-body lubrication model. *Compt Rendus Acad Sci Math*. 1997;325(9):1053-1058. https://doi.org/10.1016/S0764-4442(97)89104-5.

32. Izard E, Bonometti T, Lacaze L. Simulation of an avalanche in a fluid with a soft-sphere/immersed boundary method including a lubrication force. *J Comput Multiph Flows*. 2014;6(4):391-405. https://doi.org/10.1260/1757-482X.6.4.391.
33. Chorin AJ. Numerical solution of the Navier-Stokes equations. *Math Comput*. 1968;22(104):745-762. https://doi.org/10.1090/S0025-5718-1968-0242392-2.
34. Teman R. Appoximation of the Navier-Stokes equations by the project method (2). *Arch Ration Mech Anal*. 1969;5:351-362.
35. Schiller L, Naumann A. Fundamental calculations in gravitational processing. *Zeitschrift Des Vereines Deutscher Ingenieure*. 1933;77:318-320.
36. Brown PP, Lawler DF. Sphere drag and settling velocity revisited. *J Environ Eng*. 2003;129(3):222-231. https://doi.org/10.1061/(ASCE)0733-9372(2003)129:3(222).
37. Cadafalch J, Pérez-Segarra C, Consul R, Oliva A. Verification of finite volume computations on steady-state fluid flow and heat transfer. *J Fluids Eng*. 2002;124(1):11-21. https://doi.org/10.1115/1.1436092.
38. Roache P. Perspective: a method for uniform reporting of grid refinement studies. *J Fluids Eng*. 1994;116(3):405-413. https://doi.org/10.1115/1.2910291.
39. Mittal S, Kumar B. Flow past a rotating cylinder. *J Fluid Mech*. 2003;476:303-334. https://doi.org/10.1017/S0022112002002938.
40. Coutanceau M, Menard C. Influence of rotation on the near-wake development behind an impulsively started circular cylinder. *J Fluid Mech*. 1985;158:399-446. https://doi.org/10.1017/S0022112085002713.
41. Wan D, Turek S. Direct numerical simulation of particulate flow via multigrid FEM techniques and the fictitious boundary method. *Int J Numer Methods Fluids*. 2006;51(5):531-566. https://doi.org/10.1002/fld.1129.
42. Kajishima T, Takiguchi S, Hamasaki H, Miyake Y. Turbulence structure of particle-laden flow in a vertical plane channel due to vortex shedding. *JSME Int J Ser B Fluids Thermal Eng*. 2001;44(4):526-535. https://doi.org/10.1299/jsmeb.44.526.
43. Dong S, Liu D, Maxey MR, Karniadakis GE. Spectral distributed Lagrange multiplier method: algorithm and benchmark tests. *J Comput Phys*. 2004;195(2):695-717. https://doi.org/10.1016/j.jcp.2003.10.016.

SUPPORTING INFORMATION

Additional supporting information may be found online in the Supporting Information section at the end of this article.

How to cite this article: Reder M, Schneider D, Wang F, Daubner S, Nestler B. Phase-field formulation of a fictitious domain method for particulate flows interacting with complex and evolving geometries. *Int J Numer Meth Fluids*. 2021;93:2486–2507. https://doi.org/10.1002/fld.4984

APPENDIX A. DERIVATION OF THE DLM-METHOD

The local momentum balance for both solid and fluid in an Eulerian framework is given via

$$\partial_t(\rho\vec{u}) + \nabla \cdot (\rho\vec{u} \otimes \vec{u}) = \nabla \cdot \boldsymbol{\sigma} + \rho\vec{f}_{\mathrm{V}} \tag{A1}$$

with the mass density

$$\rho = \begin{cases} \rho_f & \vec{x} \in \Omega_{\mathrm{f}} \\ \rho_s & \vec{x} \in \Omega_{\mathrm{s}} \end{cases}$$

and the Cauchy stress tensor

$$\boldsymbol{\sigma} = \begin{cases} \boldsymbol{\sigma}_f & \vec{x} \in \Omega_{\mathrm{f}} \\ \boldsymbol{\sigma}_s & \vec{x} \in \Omega_{\mathrm{s}} \end{cases}.$$

The stress tensor in the solid arises as a Lagrange multiplier in order to fulfill the rigid body constraint. Assuming an incompressible flow of a Newtonian fluid, the stress tensor in the fluid region is given as $\boldsymbol{\sigma}_f = -p\mathbf{1} + \mu\left(\nabla\vec{u} + \nabla^T\vec{u}\right)$, where the pressure p is a Lagrange multiplier that ensures a divergence free velocity field. An integration of Equation (A1) over the domain of the pth rigid body yields

$$\frac{\mathrm{d}}{\mathrm{d}t}\int_{\Omega_p} \rho\vec{u}\,\mathrm{d}V = \int_{\partial\Omega_p} \boldsymbol{\sigma}_s\vec{n}\,\mathrm{d}S - \int_{\partial\Omega_p} \rho\vec{u}(\vec{u}^{\mathrm{rel}} \cdot \vec{n})\,\mathrm{d}S + \rho V_p\vec{g},$$

when the gravitation is the only body force $\vec{f}_{\mathrm{V}}$. The transition condition $\boldsymbol{\sigma}_f\vec{n} = \boldsymbol{\sigma}_s\vec{n}$ at the interface is exploited and since there is no mass flow over the fluid–solid interface $\vec{u}^{\mathrm{rel}} \cdot \vec{n} = 0$ holds. This results in the Newton equation for the linear momentum of the pth body

$$m_p\dot{\vec{U}}_p = \frac{\mathrm{d}}{\mathrm{d}t}\int_{\Omega_p} \rho\vec{u}\,\mathrm{d}V = \int_{\partial\Omega_p} \boldsymbol{\sigma}_f\vec{n}\,\mathrm{d}S + m_p\vec{g}. \tag{A2}$$

If a ghost fluid with the density ρ^* is considered, that obeys the NSE

$$\rho^*\dot{\vec{u}}^* = \nabla\cdot\sigma_f + \rho^*\vec{g},$$

the exact momentum balance (A1) can be rewritten by a multiplication with ρ^*/ρ, what results in

$$\begin{aligned}\rho^*\dot{\vec{u}} &= \nabla\cdot\boldsymbol{\sigma}_f - \nabla\cdot\boldsymbol{\sigma}_f + \frac{\rho^*}{\rho}\nabla\cdot\boldsymbol{\sigma} + \rho^*\vec{g}\\ &= \nabla\cdot\boldsymbol{\sigma}_f + \rho^*\vec{g} + \rho^*\vec{\lambda}^*\end{aligned} \tag{A3}$$

with the volume force

$$\rho^*\vec{\lambda}^* = \begin{cases}\vec{0} & \vec{x}\in\Omega_{\mathrm{f}}\\ \frac{\rho^*}{\rho}\nabla\cdot\boldsymbol{\sigma}_s - \nabla\cdot\boldsymbol{\sigma}_f & \vec{x}\in\Omega_{\mathrm{s}}\end{cases}. \tag{A4}$$

An integration of the momentum balance for the ghost fluid yields

$$\frac{\mathrm{d}}{\mathrm{d}t}\int_{\Omega_p} \rho^*\vec{u}^*\,\mathrm{d}V = \int_{\partial\Omega_p} \boldsymbol{\sigma}_f\vec{n}\,\mathrm{d}S + \rho^*V_p\vec{g},$$

what can be subtracted from the Newton equation (A2) resulting in

$$\frac{\mathrm{d}}{\mathrm{d}t}\int_{\Omega_p} \rho\vec{u} - \rho^*\vec{u}^*\,\mathrm{d}V = (m_p - \rho^*V_p)\vec{g} \tag{A5}$$

and thus

$$\frac{\mathrm{d}}{\mathrm{d}t}\int_{\Omega_p} \rho\vec{u}\,\mathrm{d}V = \left(1 - \frac{\rho^*}{\rho}\right)m_p\vec{g} + \frac{\mathrm{d}}{\mathrm{d}t}\int_{\Omega_p} \rho^*\vec{u}^*\,\mathrm{d}V. \tag{A6}$$

The occurring time derivatives can be approximated via

$$\partial_t(\rho\vec{u}) \approx \frac{(\rho\vec{u})^{n+1} - (\rho\vec{u})^n}{\Delta t} \qquad \text{and} \qquad \partial_t(\rho^*\vec{u}^*) \approx \frac{(\rho^*\vec{u}^*)^{n+1} - (\rho^*\vec{u}^*)^n}{\Delta t}.$$

The velocity field of the ghost fluid for the previous time step is identical to the rigid body velocity field, thus $\vec{u}^{*n} = \vec{u}_p^n = \vec{U}_p^n + \vec{\omega}_p^n \times \vec{r}$ holds. Its value of the new time step, which is subsequently shortly written as $\vec{u}^*$, represents a preliminary velocity for the rigid body domain. The DLM-method is obtained by choosing the density of the ghost fluid as $\rho^* = \rho$, what yields

$$m_p\vec{U}_p^{n+1} = \int_{\Omega_p} \rho^{n+1}\vec{u}^*\,\mathrm{d}V.$$

This corresponds to Equation (6a). In a similar fashion the equation for the angular velocity is obtained. It has to be noted, that some IBMs can be constructed with a similar approach. The choice of $\rho^* = \rho_f$ and the approximation $\partial_t\vec{u}^* = (\vec{u}^* - \vec{u})/\Delta t$ for the time derivate plugged into Equation (A6) yields

$$\dot{\vec{U}}_p = \left(1 - \frac{\rho_f}{\rho_p}\right)\vec{g} - \frac{\rho_f}{m_p\Delta t}\int_{\Omega_p} \vec{u} - \vec{u}^*\,\mathrm{d}V.$$

The barycenter velocity of the next time level can be obtained by solving this differential equation numerically and the angular momentum with a corresponding equation. This is the direct forcing method from Kajishima et al.[42] The methods from References 11,17,43 are derived by integrating the volume force (A4)

$$\begin{aligned}\int_{\Omega_p} \rho^* \vec{\lambda}^* \, \mathrm{d}V &= \frac{\rho^*}{\rho_p} \int_{\partial\Omega_p} \boldsymbol{\sigma}_s \vec{n} \, \mathrm{d}S - \int_{\partial\Omega_p} \boldsymbol{\sigma}_f \vec{n} \, \mathrm{d}S \\ &= -\left(1 - \frac{\rho^*}{\rho_p}\right) \int_{\partial\Omega_p} \boldsymbol{\sigma}_f \vec{n} \, \mathrm{d}S\end{aligned}$$

and inserting the hydrodynamic forces in the Newton equation (A2), what yields the differential equation

$$m_p \mathrm{d}_t \vec{U}_p = -\frac{\rho_p \rho^*}{\rho_p - \rho^*} \int_{\Omega_p} \vec{\lambda}^* \, \mathrm{d}V + m_p \vec{g}.$$

The density of the ghost fluid can obviously not be the same like the density of the particle. A convenient choice is $\rho^* = \rho_f$, when fluid and particle do not have the same density. The forcing term can be determined by the difference of momentum balance (A3) with the one of the ghost fluid, what results in

$$\vec{\lambda}^* = \dot{\vec{u}} - \dot{\vec{u}}^*,$$

what is typically approximated via

$$\vec{\lambda}^* = \frac{\vec{u}_p^{n+1} - \vec{u}^*}{\Delta t}.$$

APPENDIX B. EXAMINATION OF VOLUME PRESERVATION

In this part of the appendix, the different phase-field transport mechanisms introduced within this article are compared in respect to their volume preservation behavior. Therefore, a two-dimensional falling sphere problem with $Ar = 1200$ is considered, where the number of cells over the diameter is 16 and interface is resolved with 2.5 cells. The convective term in the ACE and the transport equation (12) is discretized with the van Leer flux limiter scheme, where the cell midpoint values are approximated via

$$\varphi_{i+1/2} = \varphi_i + \frac{1}{2}\Psi(\varphi_{i+1} - \varphi_i), \tag{B1a}$$

$$\Psi = \frac{\tilde{\varphi} + |\tilde{\varphi}|}{1 + \tilde{\varphi}}, \tag{B1b}$$

$$\tilde{\varphi} = \frac{\varphi_i - \varphi_{i-1}}{\varphi_{i+1} - \varphi_i}. \tag{B1c}$$

It has to be mentioned, that different schemes show qualitatively similar effects. Figure B1 shows the velocity and deviation in volume over time. For the prescribed phase-field, the volume deviation fluctuates closely around 0%, which is due to the determination of the volume via numerical integration. The preserving ACE employs a Lagrange multiplier enforcing preservation based on the numerically integrated volume and thus deviations are at scale of computational accuracy. However, the volume preservation effects the velocity, since the adjustment of eventual volume changes due to the Lagrange multiplier is applied homogeneously. Therefore, the velocity differs from the result with prescribed and purely convected phase-field with a small error far below 1% in this case. For the purely convective transport equation, it can be seen, that the volume changes over time. The magnitude of this error decreases with higher grid resolution. Still the error in volume and also the distortion of the equilibrium profile is accumulative, which is the reason why this transport equation is not employed in the article.

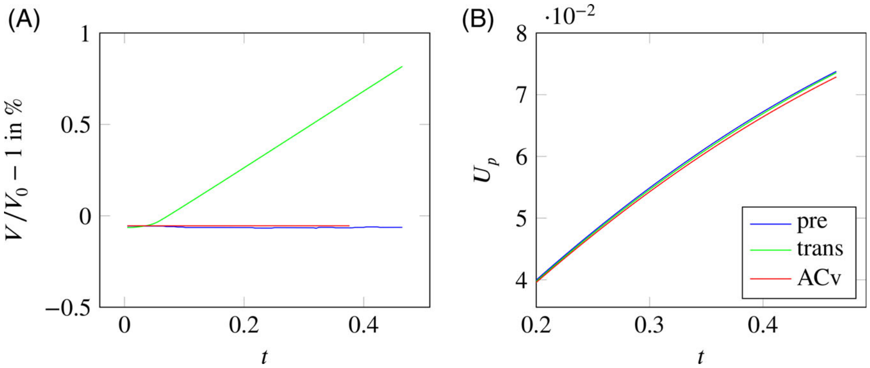

FIGURE B1 Comparison between different phase-field transport mechanisms: pre—Prescribed profile, trans—purely convective transport with van Leer flux limiter, ACv—volume preserved Allen–Cahn. (A) Relative volume change over time. (B) Velocity over time [Colour figure can be viewed at wileyonlinelibrary.com]

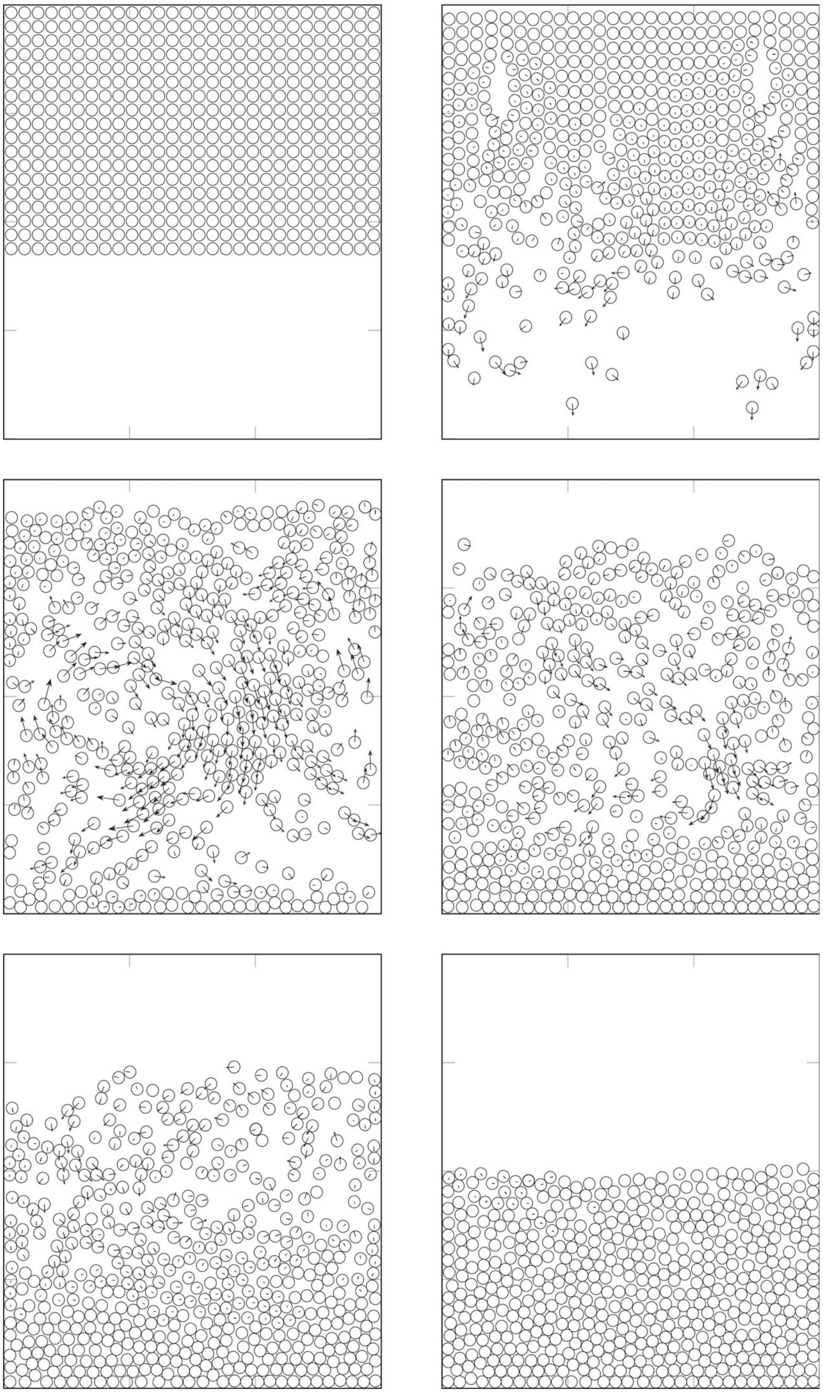

FIGURE B2 Particles with respective barycenter velocities at time step 0, 2000, 3500, 5000, 6500, and 9000 from left top to bottom right